

# A nonlinear quantum neural network framework for entanglement engineering

Adriano Macarone-Palmieri,<sup>1,\*</sup> Alberto Ferrara,<sup>1</sup> and Rosario Lo Franco<sup>1</sup>

<sup>1</sup>*Dipartimento di Ingegneria, Università degli Studi di Palermo, Viale delle Scienze, 90128 Palermo, Italy*

(Dated: December 29, 2025)

Multipartite entanglement is a key resource for quantum technologies, yet its scalable generation in noisy quantum devices remains challenging. Here, we propose a low-depth quantum neural network architecture with linear scaling with a novel approach to introducing activation functions, used for the task of entanglement engineering. As a testbed to demonstrate the clear advantage unlocked by the introduction of nonlinear activations, we run a Monte Carlo sampling over  $10^5$  circuit topologies for pure noiseless states. Supported by the clear edge offered by our approach, we focus our attention on the noisy scenario; we employ the experimentally accessible Meyer–Wallach global entanglement as a scalable surrogate optimization cost and certify entanglement using bipartite negativity. For mixed states of up to ten qubits, the optimized circuits generate substantial entanglement across both symmetric and asymmetric bipartitions. These results establish an experimentally motivated and scalable framework for engineering multipartite entanglement on near-term quantum devices, highlighting the combined role of nonlinearity and circuit topology that can achieve up to 20 qubits for very low noise levels.

## I. INTRODUCTION

Alongside quantum error correction, entanglement engineering is a cornerstone of next-generation quantum communication, sensing, and computation [1–3]. Multipartite entangled states enable enhanced security, sensitivity, and coherence, yet their scalable preparation in realistic quantum devices remains a central challenge.

Entanglement engineering can be formally cast as a graph-optimization problem, in which both interaction structure and parametrization determine the entanglement properties of the resulting quantum state [4, 5]. This perspective has motivated the use of machine-learning techniques, particularly optimization and reinforcement learning, in quantum information science [6–8]. Such approaches have been successfully applied to the automated design of quantum experiments [9], circuit synthesis [10, 11], circuit optimization [12], and the preparation and engineering of entangled states [13–15].

Quantum neural networks (QNNs) provide a flexible framework for these tasks by optimizing parametrized quantum circuits using classical learning algorithms [16]. However, most existing QNN architectures rely on strictly linear parametrizations, which limits their expressive power at fixed circuit depth. Increasing depth can partially alleviate this limitation but leads to higher hardware noise and reduced scalability, making low-depth, linearly scaling architectures particularly attractive for near-term devices [17].

A key ingredient of our approach is the introduction of different nonlinear behaviors. While nonlinear activation functions are essential for the success of classical neural networks, only a few quantum architectures incorporating nonlinearity have been explored so far [18–23]. This represents a missing yet important step in statistical learning, whose role is well established [24]. The

practical problem is that, while implementing an activation function is straightforward for classical networks, it would demand the realization of specific hardware gates and experimental solutions for a quantum network.

In this work, we address the challenge of engineering multipartite entanglement at fixed circuit depth under realistic noise by introducing a quantum neural network architecture with memory-inspired nonlinear parameter response. Rather than increasing depth or gate count, our approach exploits nonlinearity and circuit topology as complementary design resources to enhance the probability of generating highly entangled states.

To demonstrate the edge offered by our novel application of nonlinear functions, we run a Monte Carlo sampling over circuit architectures to showcase it right off from the noiseless case. To enable scalable optimization for mixed states, we employ the Meyer–Wallach global entanglement as a computationally efficient surrogate cost function, and certify entanglement using bipartite negativity. Our results establish a principled and experimentally motivated framework for multipartite entanglement engineering on near-term quantum devices, highlighting nonlinearity as a key ingredient for noisy algorithms.

We first demonstrate the edge offered by the presence of a nonlinear term, focusing mostly on simulations where the presence of noise is relevant. Our solution can be used in two ways: (i) use the training weights after the training, or (ii) directly realize it on photonic setups.

The paper is organized as follows: in Section II, we introduce the entanglement metrics, the nonlinear functions and their justification, and the gate decomposition for circuit situations. In Section III we define the model architecture, the training, and the metrics and training for the noisy scenario. Lastly, the noise gate simulates a Noise-Intermediate-Scale-Quantum (NISQ) scenario. Section IV presents the numerical results. Firstly, we offer an analysis for a pure state that demonstrates the clear boost offered by nonlinear functions. Then, we

\* [adriano.macaronepalmieri@unipa.it](mailto:adriano.macaronepalmieri@unipa.it)

focus solely on the noisy scenario. Lastly, in Section V summarizes the conclusions and outlook.

## II. PRELIMINARIES

Quantifying the degree and structure of entanglement in many-body quantum systems is essential for understanding their computational and physical capabilities [25–28]. The core idea here is to realize entangled many-body states using a nonlinear QNN, built using only one type of gate. We begin by defining the network’s building blocks: the key metric for the cost function, the new activation function strategy, and the only gate we use, which is a single photon beam-splitter-inspired gate for all our architectures. Lastly, we introduce the metric and further considerations for the NISQ scenario.

### A. The optimization metric: Meyer-Wallach Global Entanglement.

In this work, we focus on maximizing the global entanglement amount of the output state generated by each circuit topology. We use the Meyer-Wallach (MW) global entanglement measure in our optimization task [29]; this offers us two advantages by using a global validation metric: (i) they can be readily implemented inside a classical cost function; this won’t be true for mixed states, because they must be evaluated for every partition, and (ii) it offers an experimentally accessible and compact, permutation-invariant quantifier [30]. The MW is defined as follows: given a pure state  $|\psi\rangle$  of an  $N$ -qubit register, living in the Hilbert space  $\mathcal{H} = (\mathbb{C}^2)^{\otimes N}$ , the measure is defined as

$$Q(\psi) = \frac{4}{N} \sum_{i=1}^N (1 - \text{Tr}[\rho_i^2]), \quad (1)$$

where  $\rho_i = \text{Tr}_{\{1, \dots, N\} \setminus i} (|\psi\rangle\langle\psi|)$  is the reduced density operator of the  $i$ th qubit. The quantity  $\text{Tr}[\rho_i^2]$  is the purity of the reduced state, whose deviation from unity reflects the degree of mixing induced by entanglement with the rest of the register.

By construction, the measure satisfies  $0 \leq Q(\psi) \leq 1$ , with one corresponding to a maximally entangled state like the GHZ, but not a W-type state, for example. As expected, the metric vanishes if and only if the state is fully separable.

### B. Nonlinear Control Reparameterization

Generally, quantum neural networks are blocks of unitary gates trained by shifting the rotation angles  $\theta_i$  for each gate. Like their classical counterpart, they combine several elementary operations acting upon different qubits to realize different architectures. What is missing

with respect to the classical counterpart is the implementation of nonlinear activation functions. This is a concrete drawback and lies behind the great success of deep learning; therefore, its lack is a drawback in quantum machine learning. For example, a multilayer perception (MLP) reduces to a combination of matrix multiplications plus nonlinear functions right after each of them, more precisely:

$$\text{MLP}(\bar{\theta})[\mathbf{x}_{\text{in}}] = (\sigma_2 \circ W_2^{\theta_2} \circ \sigma_1 \circ W_1^{\theta_1})\mathbf{x}_{\text{in}}, \quad (2)$$

with  $\sigma_i$  a generic nonlinear function,  $\mathbf{x}_{\text{in}}$  a generic input, for a network optimizing on the set of weights parameter  $\bar{\theta}$ . In practical terms, they remap the neuron’s linear output into another space. While this can be implemented relatively simply in software, realizing a physical quantum gate that implements it is an open challenge. To tackle this setback, here we study another way around, oppositely implementing them:

$$\mathcal{U}_{\text{NN}} = \bigotimes \mathbf{U}^n(\tilde{\theta}) \cdots \mathbf{U}^1(\tilde{\theta}), \quad (3)$$

$$\tilde{\theta} = \sigma(\theta).$$

As Eq. (3) states, the activation function now modifies the output forcing it inside its dominium, and is later on linearly used by a standard gate. The first  $\sigma$  we test is inspired by a photonic quantum memristor with single photon input [21]. Given a physical-inspired reflectivity value  $R(\theta)$ , see Eq. (E1), the gate simulates an effective beam-splitter angle:

$$\tilde{\theta} = 2 \arcsin \left( \sqrt{1 - R(\theta)} \right), \quad (4)$$

which, in physical settings, determines the strength of the conditional interaction between the two modes of physical components. What is physically interesting is that this type of function brings the hallmark of quantum memory effects unraveled by a memristor-type beam-splitter. In other words, even though the gate is not implemented as a genuine memristor component, it is optimized as such.

Following Eq. (E1) and Eq. (4), we choose as the second  $\sigma_{\text{sin}}$ . This type of function draws inspiration from a recent breakthrough in the classical field of deep learning, dubbed Sinusoidal Representation Network (SIREN)[31–34]. Therefore, we also implement the SIREN-type nonlinearity:

$$\tilde{\theta} = \sin(\theta). \quad (5)$$

Last, to benchmark the advantage offered by the method, we consider the unitary function  $\bar{\theta} = 1 \cdot \theta$ .

### Photonic quantum memristor gate decomposition

– The unitary decomposition in native operations of the photonic quantum memristor (PQM) offered in [21], when restricted to only two can be decomposed using standard quantum circuit [35]:

1. A single-qubit rotation RY acting on wire A, which introduces a controlled phase accumulation proportional to the evolution time.

2. An entangling sequence modeling the beam splitter dynamics,

$$\text{CNOT}_{B \rightarrow A}, \text{CRX}_{A \rightarrow B}(-\theta), \text{CNOT}_{B \rightarrow A},$$

whose combined effect implements the reflectivity-dependent partial exchange between the two modes.

3. Last, a final SWAP gate ensures symmetry between the modes and matches the canonical ordering of a two-port beam splitter.

This entire block simulates the behaviour of a memristor-type beam splitter, as the one studied in Ref. [21]. From now on, we call this block of operations  $\mathbf{U}^{\text{BM}}$  for a gate that implements Eq. (4) as nonlinear function, and  $\mathbf{U}^{\text{sin}}$  for the one that implement Eq. (5), and in case of linear network we use standard notation  $\mathbf{U}^\theta$ ; in general we refer to it as  $\mathbf{U}^\varkappa$  where  $\varkappa = \{\text{RM}, \sin, \theta\}$ .

### III. METHODS

#### A. The architecture and optimization task

Throughout this work, we make use of the  $\mathbf{U}^\varkappa$  only to build our networks, which, in general, we define with the symbol  $\mathcal{U}_{\text{topology}}^\varkappa$ , whose definition we introduce below. Each network possesses a specific topology, which describes how each  $\mathbf{U}^{\text{BM}}$  operation (or gate) connects to couples of qubits. So, a network topology can simply be described as a list  $[(A_1, B_1) \dots (A_n, B_n)]$  to apply to our  $n$  gates. In this work, we make use of 2 key topologies, random (RN), staircase (SC):

$$\text{SC} = \mathbf{U}_{0,1}^\varkappa \mathbf{U}_{1,2}^\varkappa \dots \mathbf{U}_{n-2,n-1}^\varkappa \quad (6)$$

$$\text{RN} = \mathbf{U}_{u_0,u_1}^\varkappa \mathbf{U}_{u_1,u_2}^\varkappa \dots \mathbf{U}_{r_{n-1},r_n}^\varkappa, \quad (7)$$

with  $n$  the number of qubits[36]. The SC topology has been studied in theoretical network complexity studies to determine an optimal method to build a unitary operation from Haar-random two-qubit quantum gates [37] and is also the same implemented for linear graph states [38].

So, e.g., a network with SC topology that implements the beam-splitter type nonlinearity Eq. (4) will be written as  $\mathcal{U}_{\text{SC}}^{\text{BM}} = \bigotimes \mathbf{U}_{0,1}^{\text{BM}} \dots \mathbf{U}_{n-2,n-1}^{\text{BM}}$ . We will also consider combinations of these networks, defined when needed.

With this in hand, we can now define our entanglement generation problem as a minimization problem as follows:

$$\min_{\bar{\theta}} \left[ 1 - Q(\mathcal{U}_{\text{any}}^\varkappa(\bar{\theta}) | 0 \rangle^{\otimes n}) \right], \quad (8)$$

for *any* possible topology hereafter considered. Importantly, for the mixed state, we still employ the MW because it is a scalable, experimentally accessible surrogate cost function, whose effectiveness we validate against

negativity as a certification metric. Last, it is worth stressing the analogy with the classical counterpart; similarly to SIREN networks, a single input comprises the entire dataset.

#### B. Noisy simulation. Implementation and validation metric

To depict a more realistic scenario, it is necessary to insert noise sources at each gate level of our simulated photonic hardware. For this reason, we implement standard hardware noise sources, namely a dephasing channel after the RY, and an amplitude-damping after each wire of the simulated memristor. The noisy channel is defined as

$$\mathcal{E}_{\text{deph}}(\rho) = (1 - p)\rho + p Z \rho Z, \quad (9)$$

$$\mathcal{E}_{\text{AD}}(\rho) = K_0 \rho K_0^\dagger + K_1 \rho K_1^\dagger, \quad (10)$$

with  $Z$  the standard Pauli operator, and the Kraus matrices for the amplitude damping channel given by

$$K_0 = \begin{pmatrix} 1 & 0 \\ 0 & \sqrt{1-\gamma} \end{pmatrix}, \quad K_1 = \begin{pmatrix} 0 & \sqrt{\gamma} \\ 0 & 0 \end{pmatrix}. \quad (11)$$

To quantify the entanglement of the mixed output states, we use Entanglement negativity [39], which is an LOCC monotone, and use the positive-partial-transpose criterion [40, 41]. Given a bipartite density matrix  $\rho_{AB}$ , one performs the partial transpose with respect to subsystem  $B$ , obtaining  $\rho_{AB}^{T_B}$ . The entanglement negativity is then defined as

$$\mathcal{N}(\rho_{AB}) = \frac{\|\rho_{AB}^{T_B}\|_1 - 1}{2}, \quad (12)$$

where  $\|\cdot\|_1$  denotes the trace norm. Relative to the MW global entanglement, this is no longer interpreted as a strict entanglement monotone and an entanglement validation metric, but rather as a scalable proxy and a good surrogate cost function, promoting multipartite correlations during network optimization.

**Training hyperparameters** – For the optimization, we implement the classical Adam optimization, a learning rate of  $5 \cdot 10^{-3}$ , and early stopping for regularization. The max circuit depth considered is two. Pennylane is used to code and train all the models [42].

### IV. RESULTS

The first mandatory question to assess is the boost offered by nonlinearities inside our optimization scheme. A Monte Carlo analysis of this key question for the noiseless pure-states scenario is offered. The main outcomes hereafter displayed will leverage the numerical evidence and focus on a step-by-step analysis, starting from 5 low-noise qubits up to 10 fully noisy qubits.

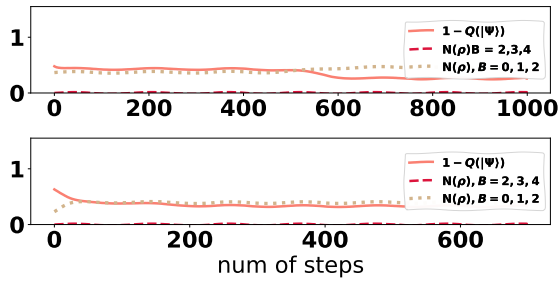


Figure 1: Upper panel. Meyer-Wallach and bipartite negativity for a single run of the  $\mathcal{U}_{sc}^{BM}$  models, i.e, the simple staircase model. Lower panel, the same plot for  $\mathcal{U}_{sc}^{sin}$  model. We can see that the optimization of this topology produces an amount of bipartite mixed state entanglement  $\sim 0.5$ , for both bipartitions, also in the presence of very low noise. This clearly prompts us to introduce more gates between nonnearest-neighbor qubits.

**Activation functions advantage** – The histograms in Fig. 6 in the Appendix 1 display the validity of our hypothesis: (i) from the Monte Carlo analysis of  $10^5$  random noiseless circuits, we show that the use of nonlinear functions offers a significant boost for the entanglement production, and (ii) in this regime, because the Meyer-Wallach is both an entanglement cost function and a valid validation metric, we can scale up to 20 qubits simply by implementing the SC topology for almost pure states, see Fig. 11.

### A. 5 qubits on low noise analysis

In this section, we analyze the networks  $\mathcal{U}_{sc}^{BM}$  and  $\mathcal{U}_{sc+1}^{BM}$  under low noise. We implement Eq. (10) to introduce an amplitude damping gate at the end of each SWAP’s wires, with a  $\gamma = 0.01$ , our numerical experiment shows that the SC topology poorly performs in this regime. Not only does the cost function minimization – which is equivalent to the Meyer Wallach maximization – not go to zero. Also, the amount of entanglement in the sub-partition is  $< 0.5$ , a low value compared to the theoretical upper bound of  $\sim 1.5$ . Instead, just by adding one connection (topology SC+1), the situation changes.

The negativity is provided for the partition  $[0, 1, 2]$  and  $[2, 3, 4]$  for an initial  $|0\rangle^{\otimes 5}$ . The theoretical upper bound for this partition is, for a pure state  $\sim 1.5$  [39].

Undoubtedly, Fig. 2 confirms the sensitivity of the network to initial parameter weights. Looking at the upper panel, we can see that  $\mathcal{U}_{sc+1}^{BM}$  is bound to achieve greater performance, a value of  $\sim 1.46$  when the theoretical upper bound is 1.5, demonstrating the efficiency of the approach for a small number of qubits. We can appreciate now how the  $\mathcal{U}_{sc+1}^{BM/sin}$  models’ standard deviation in the learning curve is evident now, of the order of  $\sim 10^{-1}$ .

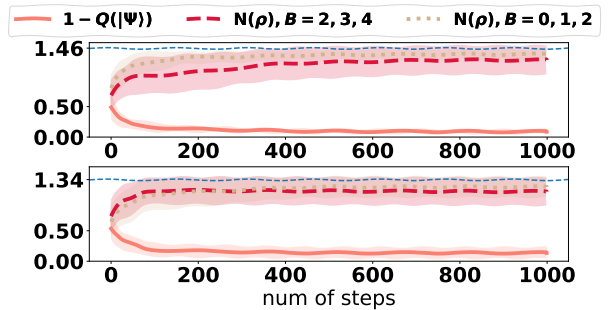


Figure 2: Upper panel. Mean value and standard deviation training evolution for 20 different random initializations of the network  $\mathcal{U}_{sc+1}^{BM}$ . Lower panel. The same for  $\mathcal{U}_{sc+1}^{sin}$  networks. In the upper panel, we can see that the memristor-inspired architecture achieves a higher standard deviation, but can potentially obtain a close-to-theoretical value for  $B=[0,1,2]$ , while this is not the case for the  $\mathcal{U}_{sc+1}^{sin}$  model. This shows the potential and the sensitivity as well to the network’s initialization values.

### B. 5 qubits NISQ scenario

To investigate the performance of the proposed architecture under realistic near-term conditions, we simulate a NISQ scenario by including both dephasing and amplitude-damping noise at the gate level. Specifically, a dephasing channel is applied immediately after each single-qubit rotation  $R_Y$  within every  $U_\kappa$  block, while amplitude damping with rate  $\gamma = 0.01$  is applied after each wire of the simulated beam-splitter operation.

As stated in Sec. III, the MW metric is now used as a valid cost function and scalable surrogate, and the multipartite entanglement is certified with bipartite negativity. We begin by considering five-qubit networks with  $U_{sc+1}^{SC+1}$  topology, with a final coupling between qubits  $(A, B) = (4, 0)$ . To assess the impact of circuit connectivity, we also introduce an enhanced topology denoted

$$\mathcal{U}_{SC+2}^{BM/sin} = \mathcal{U}_{SC+1}^{BM/sin} \otimes \mathbf{U}_{3,1}^{BM/sin}, \quad (13)$$

which increases the number of long-range interactions.

As shown in Fig. 3, under full noise, the SC + 1 topology is observed to stumble on distributing entanglement uniformly across different bipartitions, with distinct partitions converging to noticeably different negativity values. This behavior is consistent with the detrimental effect of dephasing noise on the propagation of coherent entanglement in sparsely connected circuits.

By contrast, the SC + 2 topology significantly improves both convergence and robustness. As illustrated in Fig. 4, the additional coupling enables smoother optimization dynamics and leads to comparable negativity values across complementary bipartitions. In particular, for the sinusoidal nonlinear activation, the achieved negativity approaches the corresponding theoretical upper

bound for the considered partitions, indicating the effective generation of multipartite entanglement despite the presence of noise.

These results highlight the crucial role of circuit topology in the noisy regime. While the surrogate Meyer-Wallach cost function drives the optimization, the network's ability to translate this optimization into genuine multipartite entanglement, as certified by negativity, depends sensitively on the connectivity structure. Enhanced topologies mitigate the adverse effects of local noise by facilitating entanglement redistribution across the many-body system.

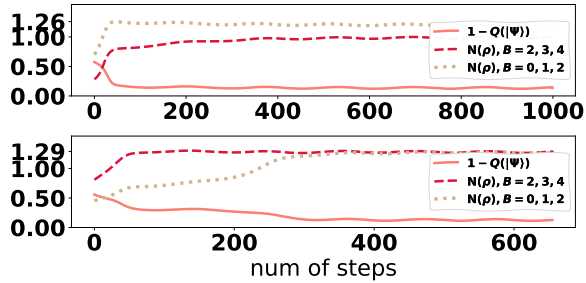


Figure 3: Full noisy simulation with dephasing channel after RY and amplitude damping after  $U_{\times}$ . Upper panel, the simulation for  $\mathcal{U}_{sc+1}^{BM}$ . We measure the negativity over two partitions, comparing it to the MW maximization. We can see that the two partitions do not achieve the same value. Lower panel. Same test but for  $\mathcal{U}_{sc+1}^{sin}$ . No significant improvement can be found.

From Fig. 3, we can see that the network struggles with preparing the entanglement on the two sub partitions, as we may expect. To counteract the detrimental effect of the dephasing noise, we add a block  $U_{\times}$  more into the network.

In Fig. 4 we can appreciate the effects of this topology in Eq. (13), whose structure is meant to stitch together the opposite qubits of our many-body state. Not only is the training smooth and faster, but, as can be noticed in the lower panel for  $\mathcal{U}_{sc+2}^{sin}$ , the two bipartitions can achieve a value of negativity which is close to the theoretical maximum of  $\sim 1.5$ .

### C. 10 qubits NISQ scenario. Topology study

Last, we scale the problem for a many-body state of 10 qubits. We opt for testing three types of networks for *sine* only nonlinear term:

$$\begin{aligned}\mathcal{U}_{10}^{[5-9]} &= \mathcal{U}_{sc+1} \mathbf{U}_{8,1} \mathbf{U}_{7,2} \cdots \mathbf{U}_{5,4} \\ \mathcal{U}_{10}^{[0-3]} &= \mathcal{U}_{sc+1} \mathbf{U}_{8,1} \mathbf{U}_{7,2} \mathbf{U}_{6,3} \mathbf{U}_{4,1} \mathbf{U}_{5,2} \\ \mathcal{W}_{10}^{[0-3]} &= \mathcal{U}_{10}^{[0-3]} \mathbf{U}_{9,1} \mathbf{U}_{8,0}\end{aligned}$$

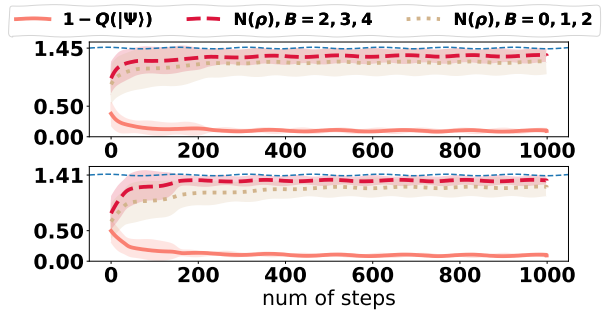


Figure 4: Mean value and standard deviation of the evolution of the full noisy simulation with dephasing channel after RY and amplitude damping after  $U_{\times}$ , for 20 different random initialization of the network. Upper panel and lower panels showing the BM and sin simulations as usual. We can observe that the  $\mathcal{U}_{sc+2}^{sin}$  can potentially achieve close to the theoretical value, and the physical memristor-inspired  $\mathcal{U}_{sc+2}^{BM}$  is bound to be slightly more efficient. This confirms the sensitivity to the network's parameter initialization values, but different from Fig. 2, this now reduces, as the difference in standard deviation demonstrates. This can be interpreted as a positive side effect of noise injection inside the differential landscape.

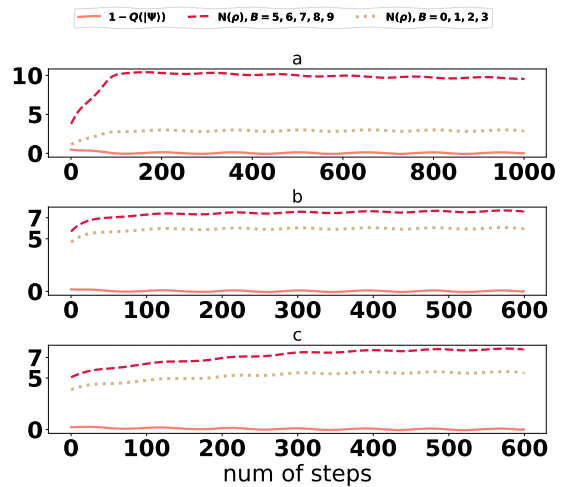


Figure 5: Panel (a). Negativity bipartite entanglement production for the  $\mathcal{U}_{10}^{[5-9]}$  network, with dephasing noise of strength  $p = 0.01$  and amplitude damping of  $\gamma = 0.01$ . For this topology, the production of entanglement for the mixed case achieves a value of  $\sim 10$  for a theoretical maximum of 15. Panel (b) and (c). Mixed states entanglement engineering for sub partition  $B=[0,1,2,3]$ , using the network  $\mathcal{U}_{10}^{[0-3]}$  and  $\mathcal{W}_{10}^{[0-3]}$ . The topology can still produce a measurable amount of entanglement for the desired bipartition, but with more effort, and obtains in panel (b) at most a value of 6 for negativity and 5.6 in panel (c). This demonstrates that introducing more gates can be detrimental for entanglement engineering in NISQ scenarios.

In Fig. 5, we can at what extent the topology design can influence the production of entanglement between bipartitions. In the plot (a), we can see the action of  $\mathcal{U}_{10}^{[5-9]}$ . Our engineering approach is particularly effective for symmetric bi-partition. Forcing the entanglement into  $B = [0,1,2,3]$ , instead, is more difficult. Comparing panel (b) with (c), we can see how the network  $\mathcal{U}_{10}^{[0-3]}$  and  $\mathcal{W}_{10}^{[0-3]}$  redistribute it. It is worth to highlight is that  $\mathcal{U}_{10}^{[0-3]}$ , in panel (b), has fewer gates, 12 instead of 14, but has better performance, obtaining  $\sim 6$  of negativity against the  $\sim 5.6$  from  $\mathcal{W}_{10}^{[0-3]}$ . So, for non-symmetric bi-partitions, increasing the number of gates does not seem to be a fruitful path.

The topology distributes the entanglement between the sub-partition  $B = [0,1,2,3,4]$ , which can achieve a value of  $\sim 10$  for a theoretical upper-bound of  $\sim 15$ , while for  $B = [0,1,2]$  we obtain a gain but a relatively small value of negativity of  $\sim 3$ . This means that the topology structure does affect the many-body properties of the outcome state.

## V. CONCLUSION

We have introduced a low-depth, linearly scaling quantum neural network architecture for entanglement engineering, inspired by memory-enabled photonic components and incorporating physically motivated nonlinear activation functions. By combining nonlinearity with simple two-qubit beam-splitter-based operations and using the Meyer-Wallach as a surrogate cost function, the proposed framework enhances the expressive power of quantum circuits without increasing circuit depth beyond linear scaling.

Through numerical simulations and Monte Carlo sampling over circuit topologies, we identified network struc-

tures capable of efficiently generating highly entangled pure states, using several two-qubit operations proportional to the system size. These results highlight the central role of nonlinearity and topology in enabling scalable multipartite entanglement generation.

We further investigated the performance of the architecture in realistic noisy scenarios. In this regime, we certify multipartite entanglement using bipartite negativity. For mixed states of up to ten qubits, the optimized circuits produce substantial entanglement across both symmetric and asymmetric bipartitions. With the symmetric case achieving a negativity of 10 for a theoretical bound of  $\sim 15$ , while for the asymmetric case, the problem is more complex, and we can achieve a  $\sim 6$  in entanglement production. Importantly, increasing the number of gates turns out as a less efficient route. This is a striking difference compared to the noiseless scenario, where increasing the number of CNOT and SWAP gates is bound to improve the amount of state entanglement. Taken together, our results establish a lightweight and experimentally motivated framework for engineering multipartite entanglement on near-term photonic platforms, in both pure and noisy quantum systems. Future endeavors will be devoted to a higher in-depth understanding, likely implementing also reinforcement learning or agentic solutions, together with a systematic effort for its theoretical description.

## ACKNOWLEDGMENTS

A.M.P. and R.L.F. acknowledge support by MUR (Ministero dell'Università e della Ricerca) through the PNRR Project ICON-Q-Partenariato EstesoNQSTI - PE00000023 - Spoke 2 - CUP: J13C22000680006.

---

[1] R. Horodecki, P. Horodecki, M. Horodecki, and K. Horodecki, Quantum entanglement, *Rev. Mod. Phys.* **81**, 865 (2009).

[2] J. Huang, M. Zhuang, and C. Lee, Entanglement-enhanced quantum metrology: From standard quantum limit to heisenberg limit, *Appl. Phys. Rev.* **11**, 031302 (2024).

[3] Z. Zhang, C. You, O. S. M. na Loaiza, R. Fickler, R. de J. León-Montiel, J. P. Torres, T. S. Humble, S. Liu, Y. Xia, and Q. Zhuang, Entanglement-based quantum information technology: a tutorial, *Adv. Opt. Photon.* **16**, 60 (2024).

[4] M. Krenn, X. Gu, and A. Zeilinger, Quantum experiments and graphs: Multipartite states as coherent superpositions of perfect matchings, *Phys. Rev. Lett.* **119**, 240403 (2017).

[5] K. Mahdavipour, F. Nosrati, S. Sciara, R. Morandotti, and R. Lo Franco, Generation of genuine multipartite entangled states via indistinguishability of identical particles, *PRX Quantum* **5**, 040350 (2024).

[6] M. Krenn, J. Landgraf, T. Foesel, and F. Marquardt, Artificial intelligence and machine learning for quantum technologies, *Phys. Rev. A* **107**, 010101 (2023).

[7] Y. Alexeev, M. H. Farag, T. L. Patti, M. E. Wolf, N. Ares, A. Aspuru-Guzik, S. C. Benjamin, Z. Cai, S. Cao, C. Chamberland, Z. Chandani, F. Fedele, I. Hamamura, N. Harrigan, J.-S. Kim, E. Kyoseva, J. G. Lietz, T. Lubowe, A. McCaskey, R. G. Melko, K. Nakaji, A. Peruzzo, P. Rao, B. Schmitt, S. Stanwyck, N. M. Tubman, H. Wang, and T. Costa, Artificial intelligence for quantum computing, *Nature Communications* **16**, 10.1038/s41467-025-65836-3 (2025).

[8] O. M. Yevtushenko and F. Marquardt, *Automated discovery of gadgets in quantum circuits for efficient reinforcement learning* (2025), arXiv:2509.24666 [quant-ph].

[9] D. Flam-Shepherd, T. C. Wu, X. Gu, A. Cervera-Lierta, M. Krenn, and A. Aspuru-Guzik, Learning interpretable representations of entanglement in quantum optics ex-

periments using deep generative models, *Nature Machine Intelligence* **4**, 544–554 (2022).

[10] S. Giordano and M. A. Martin-Delgado, Reinforcement-learning generation of four-qubit entangled states, *Phys. Rev. Res.* **4**, 043056 (2022).

[11] F. Fürrutter, G. Muñoz-Gil, and H. J. Briegel, Quantum circuit synthesis with diffusion models, *Nature Machine Intelligence* **6**, 515–524 (2024).

[12] J. Riu, J. Nogué, G. Vilaplana, A. García-Saez, and M. P. Estarellas, Reinforcement learning based quantum circuit optimization via zx-calculus, *Quantum* **9**, 1758 (2025).

[13] Z. W. Wang and Z. M. Wang, Arbitrary quantum states preparation aided by deep reinforcement learning, *Physica Scripta* **100**, 045103 (2025).

[14] Y. Qiu, M. Zhuang, J. Huang, and C. Lee, Efficient and robust entanglement generation with deep reinforcement learning for quantum metrology, *New J. Phys.* **24**, 083011 (2022).

[15] L.-L. Ye, C. Arenz, J. M. Lukens, and Y.-C. Lai, Entanglement engineering of optomechanical systems by reinforcement learning, *APL Machine Learning* **3**, 016107 (2025).

[16] M. Schuld, *Supervised quantum machine learning models are kernel methods* (2021), arXiv:2101.11020 [quant-ph].

[17] D. Luo and J. Halverson, Infinite neural network quantum states: entanglement and training dynamics, *Machine Learning: Science and Technology* **4**, 025038 (2023).

[18] L. Monbroussou, B. Polacchi, V. Yacoub, E. Caruccio, G. Rodari, F. Hoch, G. Carvacho, N. Spagnolo, T. Gordan, M. Bossi, A. Rajan, N. D. Giano, R. Albiero, F. Ceccarelli, R. Osellame, E. Kashefi, and F. Sciarrino, *Photonic quantum convolutional neural networks with adaptive state injection* (2025), arXiv:2504.20989 [quant-ph].

[19] M. Spagnolo, J. Morris, S. Piacentini, M. Antesberger, F. Massa, A. Crespi, F. Ceccarelli, R. Osellame, and P. Walther, Experimental photonic quantum memristor, *Nat. Phot.* **16**, 318–323 (2022).

[20] N. Killoran, T. R. Bromley, J. M. Arrazola, M. Schuld, N. Quesada, and S. Lloyd, Continuous-variable quantum neural networks, *Phys. Rev. Res.* **1**, 033063 (2019).

[21] A. Ferrara and R. Lo Franco, Entanglement and coherence dynamics in photonic quantum memristors, *Phys. Rev. A* **111**, 012421 (2025).

[22] S. Kumar, F. Cárdenas-López, N. Hegade, F. Albarrán-Ariagada, E. Solano, and G. A. Barrios, Tripartite entanglement in quantum memristors, *Phys. Rev. Appl.* **18**, 034004 (2022).

[23] S. Kumar, F. A. Cárdenas-López, N. N. Hegade, X. Chen, F. Albarrán-Ariagada, E. Solano, and G. Alvarado Barrios, Entangled quantum memristors, *Phys. Rev. A* **104**, 062605 (2021).

[24] V. Kunc and J. Kl'ema, Three decades of activations: A comprehensive survey of 400 activation functions for neural networks, arXiv:2402.09092 (2024).

[25] J. Sperling and W. Vogel, Multipartite entanglement witnesses, *Phys. Rev. Lett.* **111**, 110503 (2013).

[26] R. Rahimi, A. SaiToh, M. Nakahara, and M. Kitagawa, Single-experiment-detectable multipartite entanglement witness for ensemble quantum computing, *Phys. Rev. A* **75**, 032317 (2007).

[27] M. Ma, Y. Li, and J. Shang, Multipartite entanglement measures: A review, *Fundamental Research* **5**, 2489 (2025).

[28] X. Jia, C. Zhai, X. Zhu, C. You, Y. Cao, X. Zhang, Y. Zheng, Z. Fu, J. Mao, T. Dai, L. Chang, X. Su, Q. Gong, and J. Wang, Continuous-variable multipartite entanglement in an integrated microcomb, *Nature* **639**, 329–336 (2025).

[29] D. A. Meyer and N. R. Wallach, Global entanglement in multiparticle systems, *Journal of Mathematical Physics* **43**, 4273 (2002).

[30] S. Boixo and A. Monras, Operational interpretation for global multipartite entanglement, *Phys. Rev. Lett.* **100**, 100503 (2008).

[31] B. Mildenhall, P. Hedman, R. Martin-Brualla, P. P. Srinivasan, and J. T. Barron, Neural fields: A survey, Foundations and Trends in Computer Graphics and Vision **14**, 154 (2022).

[32] V. Sitzmann, J. Martel, A. Bergman, D. Lindell, and G. Wetzstein, Implicit neural representations with periodic activation functions, in *Advances in Neural Information Processing Systems*, Vol. 33, edited by H. Larochelle, M. Ranzato, R. Hadsell, M. Balcan, and H. Lin (Curran Associates, Inc., 2020) pp. 7462–7473.

[33] H. Li, Y. Miao, Z. S. Khodaei, and M. Aliabadi, Finite-pinn: A physics-informed neural network with finite geometric encoding for solid mechanics, *Journal of the Mechanics and Physics of Solids* **203**, 106222 (2025).

[34] R. Gao and R. Jaiman, H-siren: Improving implicit neural representations with hyperbolic periodic functions, arXiv:2410.04716 (2024).

[35] C. M. Dawson and M. A. Nielsen, The solovay-kitaev algorithm, *Quantum Info. Comput.* **6**, 81–95 (2006).

[36] Note that for having  $n$  applied gates, the labels must range from 0 to  $n$ .

[37] J. Haferkamp, P. Faist, N. B. T. Kothakonda, J. Eisert, and N. Yunger Halpern, Linear growth of quantum circuit complexity, *Nature Physics* **18**, 528–532 (2022).

[38] M. Hein, J. Eisert, and H. J. Briegel, Multiparty entanglement in graph states, *Phys. Rev. A* **69**, 062311 (2004).

[39] G. Vidal and R. F. Werner, Computable measure of entanglement, *Phys. Rev. A* **65**, 032314 (2002).

[40] A. Peres, Separability criterion for density matrices, *Phys. Rev. Lett.* **77**, 1413 (1996).

[41] M. Horodecki, P. Horodecki, and R. Horodecki, Separability of mixed states: necessary and sufficient conditions, *Physics Letters A* **223**, 1 (1996).

[42] V. Bergholm, J. Izaac, M. Schuld, C. Gogolin, S. Ahmed, V. Ajith, M. S. Alam, G. Alonso-Linaje, B. Akash-Narayanan, A. Asadi, J. M. Arrazola, U. Azad, S. Banning, C. Blank, T. R. Bromley, B. A. Cordier, J. Ceroni, A. Delgado, O. D. Matteo, A. Dusko, T. Garg, D. Guala, A. Hayes, R. Hill, A. Ijaz, T. Isacsson, D. Ittah, S. Jhangiri, P. Jain, E. Jiang, A. Khandelwal, K. Kottmann, R. A. Lang, C. Lee, T. Loke, A. Lowe, K. McKiernan, J. J. Meyer, J. A. Montañez-Barrera, R. Moyard, Z. Niu, L. J. O'Riordan, S. Oud, A. Panigrahi, C.-Y. Park, D. Polatajko, N. Quesada, C. Roberts, N. Sá, I. Schoch, B. Shi, S. Shu, S. Sim, A. Singh, I. Strandberg, J. Soni, A. Száva, S. Thabet, R. A. Vargas-Hernández, T. Vincent, N. Vitucci, M. Weber, D. Wierichs, R. Wiersema, M. Willmann, V. Wong, S. Zhang, and N. Killoran, *Pennylane: Automatic differentiation of hybrid quantum-classical computations* (2022), arXiv:1811.04968 [quant-ph].

[43] A. Suprano, D. Zia, L. Innocenti, S. Lorenzo, V. Ci-

mini, T. Giordani, I. Palmisano, E. Polino, N. Spagnolo, F. Sciarrino, G. M. Palma, A. Ferraro, and M. Paternostro, Experimental property reconstruction in a photonic quantum extreme learning machine, *Phys. Rev. Lett.* **132**, 160802 (2024).

[44] L. Innocenti, S. Lorenzo, I. Palmisano, A. Ferraro, M. Paternostro, and G. M. Palma, Potential and limitations of quantum extreme learning machines, *Commun. Phys.* **6**, 10.1038/s42005-023-01233-w (2023).

## 1. Pure states random topologies analysis

Because each different topology can give rise to a different output state, the first question to answer is "how many useful topologies may we expect?". To look into this, we run an exploratory Monte Carlo analysis sampling  $10^5$  RN topologies, for a 5-qubit and  $\mathcal{U}_{\text{RN}}^{\text{BM}}$  and  $\mathcal{U}_{\text{RN}}^{\theta}$  models. As Fig.6 unfolds, the nonlinear components un-

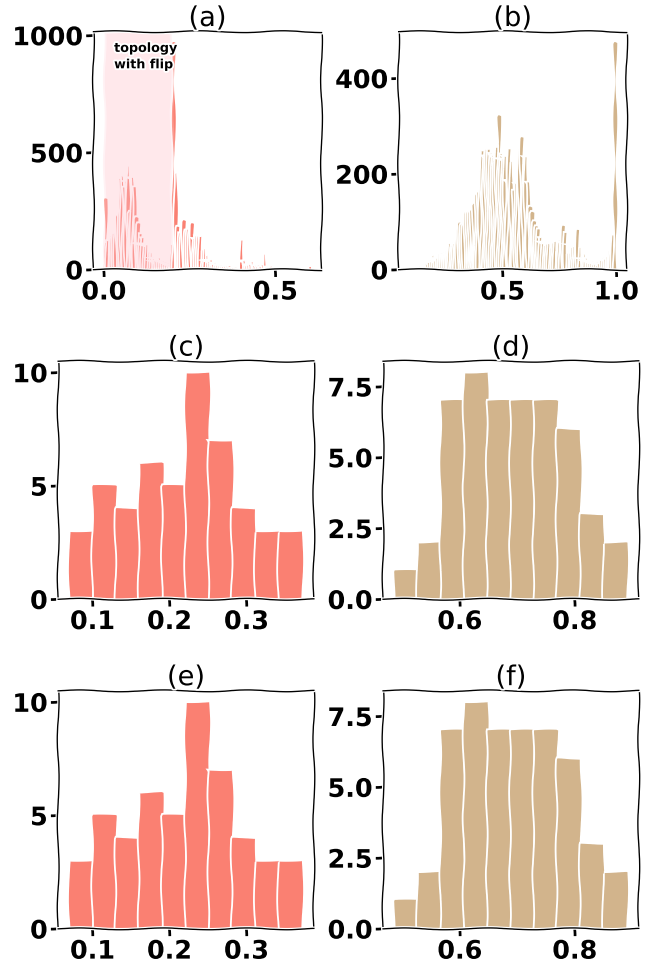


Figure 6: Panels (a) (b). Histogram of the loss function achieved by a total of  $10^5$  random  $\mathcal{T}$  for 5 qubits. Panels (c) (d), histogram for 60 for 11 qubits. We compare the  $\mathcal{U}_{\text{sc+1}}^{\text{RN}}$  (red bars) against  $\mathcal{U}_{\text{RN}}^{\theta}$  (yellow bars). The network loss function maximizes the MW values of the output states by minimizing Eq. 8. So, values close to zero in the loss function indicate higher values of global entanglement in the output pure state. We can clearly see that the presence of a nonlinearity as given by Eq. F2 response function, unlocks a greater optimal minima search.

lock better outcomes, with many more random QNN that can achieve values of MW above 0.8. This fact can be leveraged to prepare a training dataset for classical deep learning solutions meant to synthesize optimal topologies. We also run a quick analysis for a small noise

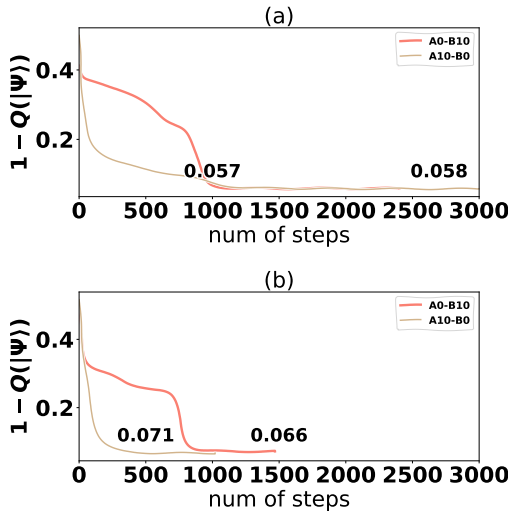


Figure 7: Panel (a). Optimization history – the Meyer-Wallach entanglement maximization – for the  $\mathcal{U}_{sc+1}^{BM}$  and  $\mathcal{W}_{sc+1}^{BM}$  architecture with for a 11 qubits quantum network. Panel (b). The  $\mathcal{U}_{sc+1}^{sin}$  and  $\mathcal{W}_{sc+1}^{sin}$  architectures outcomes. The beam-splitter nonlinearity term brings a slightly better performance, but the *sin* term leads to a faster convergence. This may point out a better fitness of the *sine* nonlinear term, for general cases, like the noisy one.

scenario, where only amplitude damping is considered. Again, we confirm that the presence of nonlinear functions is necessary to achieve higher performances; the results are shown in Sec.B. Another natural question that arises is the dependency of the networks on initial conditions and parameter variation, i.e., the  $T_{osc/int}$  that describes the physical gate, even though we are in a noiseless case. Results of the noiseless study can be found in A and show that for this scenario, no dependency is found. **The topologies of 0.8 threshold** – As shown in panel (a), the MW value of 0.8 turns out as a threshold, or a specific boundary when a transition occurs. We analyze the structure of topologies below 0.8 and found that all of them have at least one wire set (A,B) with  $A > B$  and that connect qubits that are not neighbors. This will play a critical role in Sec. IV B when the presence of noise will be investigated.

## 2. Scale-up and the sinusoidal hypothesis

The nonlinear function in Eq. (4) records the memory behaviour of a quantum memristor element, when a sinusoidal input is used in input. Here, we want to both (i) scale-up the problem and (ii) compare the model  $\mathcal{U}_{sc+1}^{BM}$  versus  $\mathcal{U}_{sc+1}^{sin}$ , bridging with SIREN classical networks. To address both questions, we display the learning curve for  $11\mathcal{T}_{ladder}$ . For this experiment, we consider two topologies  $\mathcal{U}_{sc+1}^{BM/sin} = \mathcal{U}_{sc}^{BM/sin} \otimes \mathbf{U}_{10,0}^{BM/sin}$  and

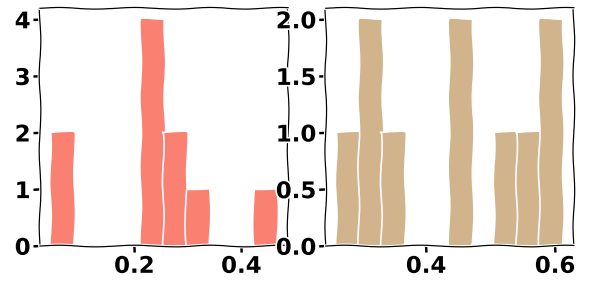


Figure 8: Histograms of 10 random topologies with amplitude noise on each wire after the SWAP gate that simulate the  $\mathbf{U}^{\infty}$ . Left histogram,  $\mathcal{U}_{RN}^{BM}$ . right histogram, the  $\mathcal{U}_{RN}^{\theta}$  random topologies are compared. Also, for moderate noise, the better performances obtained from a nonlinear function are evident with minimal sampling.

$$\mathcal{W}_{sc+1}^{BM/sin} = \mathcal{U}_{sc} \otimes \mathbf{U}_{0,10}^{BM/sin}.$$

For 11 qubits, Eq. 4 and Eq. 5 are numerically equivalent. This means that sinusoidal nonlinear functions are a valuable tool in our task of entanglement engineering, and the analogy with the SIREN is well-posed. The only appreciable difference between the two terms is the number of epochs (steps) needed to achieve convergence. The *sine* function offers a faster convergence; this can be the hallmark of a potential term with better fitness to our optimization problem. To conclude, we run the same analysis for 20 qubits either; this can be found in D.

## Appendix A: Initial condition dependency

For both quantum and classical models, if the differential landscape is not smooth, the solution may oscillate due to the initial set of random weights used to initialize them. In this section we study how changes in the leading physical values of Eq. E1 may affect the final outcomes of the network. We choose  $T_{osc}/T_{osc} = [0.2, 0.5, 0.8, 1.1, 1.4]$ . We fix the network choosing  $\mathcal{U}_{ladder}$ , both noise and noiseless, then run for each pair  $(T_{osc}, T_{int})$  20 optimization runs, to calculate the mean and variance obtained for each combination. The key result is that the variance, in both noisy and noiseless scenarios, is below  $10^{-8}$ , while the mean value ranges between  $0.07 - 0.03$  and  $0.11 - 0.06$  for the noiseless and noisy scenarios, respectively. This is likely due to the linear complexity of the network, which needs to optimize a small number of parameters. Therefore, the differential landscape is very smooth.

## Appendix B: 5 noisy gates analysis

In this last round of experiments, we consider the situation where an amount of photon loss, here modeled using an amplitude damping channel with  $\gamma = 0.001$ , is

added at the end of each gate on both wires. We sample ten random topologies and use them to run two Even though the number of topologies here sampled is pretty low, we can immediately find one that can obtain entanglement values of 0.07 and 0.31 for the memristor type, and 0.09 and 0.16 for the sine nonlinear element. The same outcomes are also confirmed for SC+1 in Fig.9.

In the second histogram, we display the result obtained for the architecture  $\mathcal{U}_{\text{RN}}^{\text{sin}}$  topology, compared against its  $\mathcal{U}_{\text{RN}}^{\theta}$  counterpart.

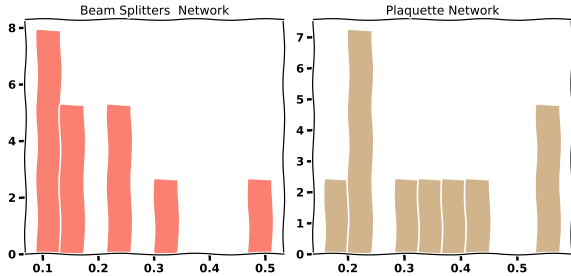


Figure 9: Histogram for 10 different random topologies for a 5-qubit neural network. On the left, the  $\mathcal{U}_{\text{RN}}^{\text{sin}}$  structure, and on the right, the  $\mathcal{U}_{\text{RN}}^{\theta}$  model sharing same RN topologies. The sin model is pretty much equivalent to the beam-splitter, but always superior to the linear one.

We can notice again that the hypothesis that the sine nonlinear components offer an evident advantage, and undoubtedly, for the global entanglement generation problem, this family of nonlinearity bestows high efficiency. Compared to Fig.8 we can appreciate that both  $\mathcal{U}_{\text{sc+1}}^{\text{BM}}$  and  $\mathcal{U}_{\text{sc+1}}^{\text{sin}}$  are comparable.

### Appendix C: 10 qubits with amplitude damping noise

In this section, we provide the outcomes obtained from the MW optimization for 10 qubits with  $\mathcal{U}^{\text{BM}(t)}$  and  $\mathcal{U}^{\text{sin}(t)}$ , and  $\mathcal{T}_{\text{ladder}}$ . We can see that the topology close to the linear graph state is extremely efficient and can achieve a value of MW close to a GHZ.

In this numerical experiment, we can see the entanglement engineering ability obtained from a 10-qubit network of  $\mathcal{U}_{\text{sc+1}}^{\text{BM}}$ . The network oscillates around the optimal minima, and obtains a value of  $\sim 0.98$  of MW entanglement, and  $\sim 0.75$  for the  $\mathcal{U}_{\text{sc+1}}^{\text{BM}}$  and  $\mathcal{U}_{\text{sc+1}}^{\text{sin}}$  models respectively. The memristor reflectivity enhanced a greater stability inside the training, enabling the early-stopper to operate and stop the simulation before reaching 2000 epochs.

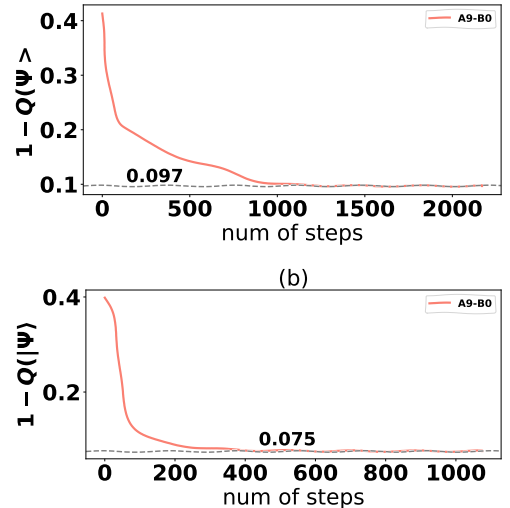


Figure 10: Panel (a). The 10 qubits  $\mathcal{U}_{\text{sc+1}}^{\text{BM}}$  model for amplitude damping only with  $\gamma = 0.01$ . The mild amount of noise does not hamper the global entanglement generation. Panel(b) the  $\mathcal{U}_{\text{sc+1}}^{\text{sin}}$  ladder model. We can notice that the *sine* nonlinear function provides faster convergence to the minima.

### Appendix D: 20 qubits experiment

An open question is how the scaling in the number of qubits may affect the outcomes. In Fig.11 we compare the beam splitter nonlinear function (upper panel) against the simple sinusoidal (lower panel). This simulation is provided for a very low amount of noise, with only amplitude damping after the two SWAPs for a  $\gamma = 10^{-3}$ .

For almost pure and pure states, the memristor-inspired term in Eq. (4) offers better performance in general. We have already detailed in Sec.III that this does not hold anymore for the realistic noisy case, where now the differential panorama is completely modified by the presence of local noise.

### APPENDIX: TECHNICAL DERIVATION AND INTERPRETATION OF THE RESPONSE FUNCTION

In recent years, a revival of photonic applications to extracting quantum state properties (or features) is showing a resurgence, with several works on photonic platforms [19, 43, 44].

### Appendix E: The beam splitter reflectivity

In this work, we initiate our analysis by adopting a circuit-based model of a photonic quantum memristor, as

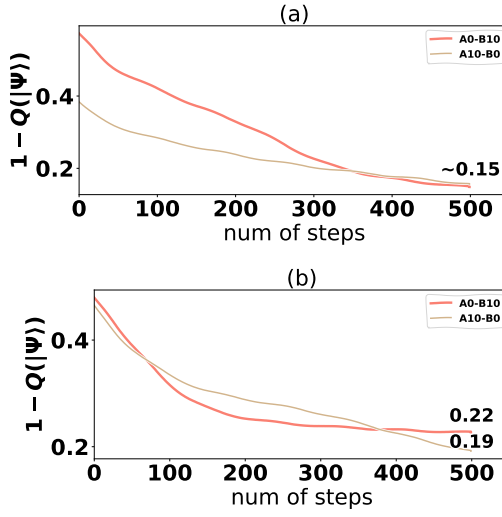


Figure 11: 20 qubit optimization. Upper panel, quantum network optimization with memristor-inspired reflectivity term. We can see that both topologies are equivalent. Lower panel, sinusoidal nonlinear term application. We can check that the topology with the control term in the last wire (number zero) is bound to achieve a higher amount of entanglement.

presented in the recent study [21]. The response function

$$R(t) = \frac{T_{\text{osc}}}{T_{\text{int}} 4\pi} \left[ \sin\left(\frac{2\pi t - 2\pi T_{\text{int}}}{T_{\text{osc}}}\right) - \sin\left(\frac{2\pi t}{T_{\text{osc}}}\right) \right], \quad (\text{E1})$$

encapsulates the temporal behaviour of an oscillatory system whose dynamics are influenced by a finite integration window  $T_{\text{int}}$  and an intrinsic oscillation period  $T_{\text{osc}}$ . The term  $\sin[(2\pi t - 2\pi T_{\text{int}})/T_{\text{osc}}]$  corresponds to the oscillation evaluated one integration interval prior, thereby encoding the system's memory of past dynamics, whereas  $\sin[(2\pi t)/T_{\text{osc}}]$  represents the instantaneous, undelayed oscillatory component. Accordingly, the function  $R(t)$  serves as a precise indicator of both residual coherence and the temporal modulation imparted by memristive dynamics, embodying the hallmark history-dependent behaviour of memory-enabled quantum systems.

#### Appendix F: Structure of the Response Function

The response function considered in the main text,

$$R(t) = \frac{T_{\text{osc}}}{T_{\text{int}} 4\pi} \left[ \sin\left(\frac{2\pi t - 2\pi T_{\text{int}}}{T_{\text{osc}}}\right) - \sin\left(\frac{2\pi t}{T_{\text{osc}}}\right) \right], \quad (\text{F1})$$

emerges from the evaluation of an oscillatory process over a finite memory window of temporal width  $T_{\text{int}}$ . This structure reflects the difference between two phase-shifted sinusoidal components, each normalized by an

amplitude factor depending on both the oscillation period and the effective integration interval.

To understand Eq. (F1), we begin by noting that an ideal periodic signal of angular frequency

$$\omega = \frac{2\pi}{T_{\text{osc}}},$$

is integrated over the shifted interval  $[t - T_{\text{int}}, t]$ . For an oscillatory function of the form  $f(\tau) = \sin(\omega\tau)$ , the finite-time integral can be computed exactly:

$$\int_{t-T_{\text{int}}}^t \sin(\omega\tau) d\tau = \frac{1}{\omega} [\cos(\omega(t - T_{\text{int}})) - \cos(\omega t)]. \quad (\text{F2})$$

Using trigonometric identities and normalizing by  $T_{\text{int}}$ , one obtains a difference of sines whose argument is shifted by  $T_{\text{int}}$ , leading to the structure displayed in Eq. (F1). The prefactor

$$\frac{T_{\text{osc}}}{T_{\text{int}} 4\pi} = \frac{1}{2\omega T_{\text{int}}},$$

arises naturally from the integral of the sinusoid and provides the correct amplitude scaling.

#### Physical Interpretation

In systems exhibiting memory-dependent (or “memristive”) behavior, the present response does not depend solely on the instantaneous value of the driving field, but also on its history within a specific temporal window. Eq. (F1) captures exactly this effect:  $R(t)$  measures the deviation introduced by integrating the oscillatory signal over an interval  $T_{\text{int}}$ , effectively encoding a temporal “lag” between the free oscillation and its memory-processed counterpart.

The two sinusoidal terms in  $R(t)$  may be interpreted as:

$$\sin[(2\pi t)/T_{\text{osc}}] \sin[(2\pi t - 2\pi T_{\text{int}})/T_{\text{osc}}], \quad (\text{F3})$$

With the first equation, the instantaneous oscillation of the underlying coherent process, and the second equation the oscillation evaluated one integration window earlier. The difference between these terms provides a direct measure of the accumulated phase displacement induced by memory effects. In oscillatory regimes where  $T_{\text{int}} \ll T_{\text{osc}}$ , this phase shift is small, and  $R(t)$  behaves nearly linearly in  $T_{\text{int}}$ . Conversely, when  $T_{\text{int}}$  becomes comparable to  $T_{\text{osc}}$ , the interference between the two sinusoidal contributions becomes pronounced, generating richer dynamical features in  $R(t)$ .

This formulation offers a compact yet powerful tool to quantify the interplay between coherence, periodic driving, and memory depth. In the context of photonic or quantum memristive systems, the response function Eq. (F1) is particularly useful for characterizing the temporal retention of coherence and for distinguishing between purely dissipative and genuinely history-dependent dynamics.

### Relevance for Memory-Dependent Quantum Dynamics

The structure of  $R(t)$  is particularly valuable for analyzing coherence in systems where memory effects play a central role, such as photonic quantum memristors.

The finite-time integral embedded in Eq. (F1) offers a tractable way to quantify temporal correlations and phase retention in the presence of noise, dissipation, or feedback, making the response function a crucial diagnostic for experimental implementations of quantum devices with non-Markovian behaviour.